

PatchDenoiser: Parameter-efficient multi-scale patch learning and fusion denoiser for medical images

Jitindra Fartiyal, Pedro Freire, Sergei K. Turitsyn, Sergei G. Solovski

February 2026

Abstract

Medical images play a critical role in clinical visualization, supporting disease diagnosis and monitoring, treatment planning, emergency care, and biomedical research. However, image quality is often degraded by noise arising from low-dose acquisition protocols, patient motion, or inherent scanner limitations, which can compromise diagnostic accuracy and negatively affect downstream image analysis. Conventional denoising approaches, such as filtering-based methods, frequently lead to excessive smoothing and loss of fine anatomical details. More recent deep learning-based techniques, including convolutional neural networks, generative adversarial networks, and transformer-based models, may help to overcome some of these limitations, but often struggle to preserve fine anatomical details or require large-scale models with substantial computational and energy costs, limiting their practicality in clinical settings.

To address these challenges, we propose PatchDenoiser, a lightweight and energy-efficient multi-scale, patch-based denoising framework. PatchDenoiser decomposes the denoising task into local texture extraction and global context aggregation, which are subsequently fused through a spatially aware patch fusion strategy. This design enables effective noise suppression while preserving fine structural and anatomical details. The proposed model is designed to be ultra-lightweight, achieving significantly fewer parameters and substantially lower computational complexity compared to existing CNN-, GAN-, and transformer-based denoising approaches.

Extensive experiments on the 2016 Mayo Low-Dose CT dataset demonstrate that PatchDenoiser consistently outperforms state-of-the-art CNN- and GAN-based methods in terms of PSNR and SSIM. The proposed framework also exhibits strong robustness across variations in slice thickness, reconstruction kernels, and Hounsfield unit (HU) windows, and generalizes effectively to cross-scanner data without requiring fine-tuning. Moreover, PatchDenoiser achieves approximately $9\times$ fewer parameters and $27\times$ lower energy consumption per inference compared with conventional CNN-based denoisers, underscoring its practical suitability for deployment in clinical AI pipelines.

Overall, PatchDenoiser offers a balanced combination of denoising performance, robustness, and computational efficiency, making it a practical and scalable solution for medical image denoising in clinical settings. The source code is publicly available at: <https://github.com/JitindraFartiyal/PatchDenoiser>.

1 Introduction

Medical images play a vital role in disease diagnosis, health monitoring, treatment planning, and a wide range of clinical applications. They also form the foundation of many artificial intelligence (AI)-based tasks, including disease detection, anatomical and pathological segmentation, and broader healthcare research. However, medical images are frequently degraded or corrupted by noise arising from factors such as low-quality or low-dose acquisition protocols, patient motion, hardware constraints, and inherent scanner limitations. The presence of noise can impede accurate diagnosis and treatment planning and can significantly degrade the performance of downstream image analysis algorithms [1], [2]. Therefore, effective noise removal is a critical preprocessing step in medical image analysis pipelines.

Noise removal becomes particularly important in the case of computed tomography (CT). CT scans expose patients to ionizing radiation, which may pose long-term health risks. To reduce radiation exposure, low-dose CT (LDCT) acquisition protocols are commonly adopted. Although LDCT improves patient safety, it introduces substantial noise into the images, making clinical interpretation and diagnosis more challenging. Consequently, effective denoising methods are essential to improve LDCT image quality while preserving diagnostically relevant structures.

Traditional noise removal techniques, such as filtering-based methods, can suppress noise but often over-smooth medical images, leading to the loss of fine anatomical details [3]. With the recent development of convolutional neural networks (CNNs), CNN-based denoisers have demonstrated improved denoising performance with reduced smoothing compared to traditional approaches. However, CNN-based methods can still produce over-smoothed patches, which reduces the visibility of small vessels and subtle tissue structures. More recently, transformer-based and generative adversarial network (GAN)-based denoisers have been proposed to alleviate excessive smoothing and improve perceptual quality. Despite these advances, such models are typically large and computationally expensive, requiring substantial training data and extensive fine-tuning [4]. Furthermore, recent studies report limited generalizability across different scanners, acquisition protocols, and clinical conditions. In summary, existing approaches face a trade-off between relatively lightweight CNN-based models with limited performance and highly complex transformer or GAN based models with large parameter counts and data requirements.

At the same time, research in deep learning architectures is approaching a point where increases in model complexity lead to disproportionately high energy consumption. For denoising tasks that often serve as a preprocessing

component within larger AI-based medical analysis pipelines, it is critical that models are lightweight, energy-efficient, robust, and generalizable, while still achieving high denoising performance. To address these challenges, we propose a new CNN-based denoising architecture based on patch-based learning. The proposed model is ultra-lightweight, with approximately nine times fewer parameters and approximately twenty-seven times lower energy consumption than traditional CNN-based architectures, while achieving state-of-the-art performance in terms of peak signal-to-noise ratio (PSNR) and structural similarity index (SSIM).

The main contributions of this work are as follows:

- We propose a multi-scale patch-based denoising framework that learns from individual patches while preserving spatial information.
- We introduce an efficient spatial-aware patch fusion strategy that integrates information from different scale patches.
- We design a parameter and energy efficient denoising model that, to the best of our knowledge, is the smallest and most energy-efficient model achieving state-of-the-art performance.
- We demonstrate the robustness and generalizability of the proposed model through extensive experiments under varying Hounsfield unit (HU) windows, kernel thicknesses, sharpness levels, and across multiple scanner test sets.

2 Related Works

Prior to the deep learning revolution, window-based filtering denoisers were widely used. These methods include mean, median, and Gaussian filtering, where each pixel is replaced by the average or statistically computed value within an $N \times N$ window. Such approaches are simple and computationally efficient; however, window-based averaging leads to excessive smoothing and loss of fine structural details. To capture non-local information in images, the non-local means (NLM) algorithm [5] was introduced, which extends beyond the local neighborhood by identifying and averaging similar patches across the image. Block-matching and 3D filtering (BM3D) [6] further improves upon this idea by grouping similar blocks into 3D volumes and performing collaborative filtering in the transform domain, followed by inverse transformation. Although NLM and BM3D outperform window-based filtering methods, they still suffer from smoothing artifacts, increased algorithmic complexity, and limited ability to accurately preserve global structural details.

Compared to traditional algorithms, deep learning-based methods have demonstrated a substantial performance improvement, particularly in capturing global structures and complex anatomical patterns. For example, RED-CNN [7] is a popular CNN-based denoising model that adopts a symmetric autoencoder architecture with residual shortcut connections to improve feature propagation.

The Dynamic Residual Attention Network (DRAN), introduced by Sharif et al. [8], incorporates dynamic convolution operations with spatial attention mechanisms to reduce excessive smoothing. Furthermore, Sharif et al. [9] proposed a cascaded two-stage framework that integrates residual dense blocks with a noise-aware attention module for more accurate pixel-wise noise estimation. In the context of ultrasound imaging, the feature-driven convolutional network (FDCCN) [10] exploits guided backpropagation and dilated convolutions to enhance despeckling performance. To strengthen multi-scale feature representation, Yang et al. [11] proposed a dual-network strategy consisting of a Feature Refinement Network (FRN) and a Dynamic Perception Network (DPN). Overall, CNN-based denoising algorithms outperform traditional methods by better preserving structural integrity; however, despite reduced smoothing compared to classical approaches, denoised images can still exhibit excessive smoothness and loss of high-frequency details.

To further mitigate smoothing artifacts, several generative adversarial network (GAN)-based, and transformer-based methods have been proposed. One notable work is CNCL by Genf et al. [12], which introduces separate models for noise and content components that are fused and evaluated using a PatchGAN discriminator, thereby avoiding conventional L1/L2-driven objectives. Extending this dual-signal concept, Huang et al. [13] proposed a dual-domain GAN architecture operating in both image and gradient spaces to better preserve edges and fine details. Adversarial and structural loss functions have also been explored, such as the GAN-based ultrasound despeckling method proposed by Mishra et al. [14], which reduces smoothing introduced by conventional loss functions while improving visual fidelity. Despite these improvements, GAN-based models remain challenging to train, are computationally expensive, and are prone to generating hallucinated or novel artifacts.

More recently, transformer-based denoising models have been investigated. CSFormer [15] enhances denoising performance by integrating cross-scale feature fusion with Swin Transformer blocks, enabling the modeling of both local textures and long-range dependencies. Another transformer-based model, CTFormer [16], utilizes token rearrangement strategies to jointly encode local texture information and global contextual interactions. Compared to GAN-based methods, transformer-based models are less prone to introducing novel artifacts and generally achieve improved visual fidelity with reduced smoothing compared to CNN-based models. However, transformer-based approaches typically require large-scale training datasets, are susceptible to overfitting, and incur high computational and training costs.

In summary, deep learning-based denoising models outperform traditional algorithms in both noise suppression and structural preservation. Among these approaches, CNN-based models are simpler and faster to train but remain susceptible to over-smoothing, whereas more complex GAN-based and transformer-based models alleviate smoothing at the cost of increased model complexity and computational overhead. Furthermore, fair and accurate comparison among existing methods remains challenging due to the lack of standardized evaluation datasets and benchmarking protocols. Several studies rely on private datasets,

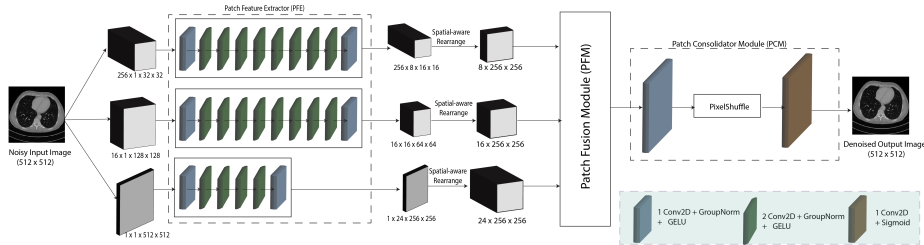


Figure 1: Overview of the PatchDenoiser framework showing the three main modules: Patch Feature Extractor (PFE), Patch Fusion Module (PFM), and Patch Consolidator Module (PCM).

limiting reproducibility, while others perform limited evaluations across acquisition parameters, making it difficult to assess generalizability. Consequently, the performance gains reported by GAN and transformer based approaches may be dataset or model specific and lack sufficient evidence of robust generalization.

These limitations motivate the need for a denoising framework that combines the efficiency of CNN-based models with improved multi-scale representation and reduced smoothing, without incurring the computational overhead of GAN or transformer-based approaches.

3 Method

PatchDenoiser is a CNN-based, spatial-aware, multi-scale denoising architecture designed to achieve high performance with a reduced number of parameters. Although image denoising is primarily a local operation, global interactions still play an important role in preserving structural consistency. Conventional CNN-based models, particularly those trained on patches, often fail to adequately capture such global interactions. PatchDenoiser addresses this limitation by structurally separating local texture extraction from global feature integration. The architecture captures local textures through patch-level processing and subsequently fuses information across scales to model global interactions.

PatchDenoiser consists of three main modules: the Patch Feature Extractor (PFE), the Patch Fusion Module (PFM), and the Patch Consolidator Module (PCM). The PFE extracts noise-free content from image patches at multiple scales. The PFM fuses information from lower-scale patches to higher-scale patches in a spatially aware manner, enabling effective cross-scale information flow. Finally, the PCM consolidates the fused feature maps and removes patch boundary artifacts to produce the final denoised output. Figure 1 illustrate the overall PatchDenoiser architecture.

3.1 Patch Feature Extractor (PFE)

At the input stage, patches of multiple scales are generated from the image. To capture both small and large-scale features, patch sizes are determined by dividing the image resolution by 16, 8, and 1. For example, for an input image of size 512×512 , patch sizes of 32×32 , 128×128 , and 512×512 are used. Instead of employing a single PFE configuration for all patch sizes, PatchDenoiser utilizes PFEs with different depths and latent dimensions.

For small patch sizes (e.g., 32×32), a deeper PFE with a smaller latent dimension is used. Since small patches contain limited contextual information, increased depth helps extract meaningful representations, while a reduced latent dimension is sufficient due to the lower information content. In contrast, for large patch sizes (e.g., 512×512), a shallower PFE with a larger latent dimension is employed to better capture global contextual information.

In addition, different kernel sizes are used at the initial layer for different patch scales, specifically kernel sizes of 3, 7, and 11 for patch sizes of 32, 128, and 512, respectively. Larger kernels for larger patch sizes enable more effective capture of global features. Unlike conventional autoencoder architectures, the spatial resolution is not aggressively reduced; instead, the spatial dimension is preserved at half of the input resolution at the output of the PFE. This structurally defined design helps minimize information loss while achieving parameter efficiency.

3.2 Patch Fusion Module (PFM)

Following the PFE stage, feature maps corresponding to different patch scales are obtained. These multi-scale feature maps are then fused using a spatially aware fusion strategy, in which lower-scale feature maps are integrated with higher-scale feature maps based on their spatial positions. This design ensures proper alignment and information flow across scales.

Fusion is performed using a gated fusion mechanism, where a sigmoid activation functions as a gate to regulate the contribution of each feature map. Fusion occurs across all PFE outputs to produce a single fused representation. The resulting fused feature map is then passed to the Patch Consolidator Module. The structural fusion process implemented in the PFM is illustrated in Figure 2

3.3 Patch Consolidator Module (PCM)

The fused output produced by the PFM already contains denoised image content; however, due to patch-based processing, residual patch boundary artifacts may still be present. The Patch Consolidator Module is a lightweight module composed of convolutional and upsampling layers designed to remove these artifacts. By refining spatial continuity across patch boundaries, the PCM produces the final denoised output image.

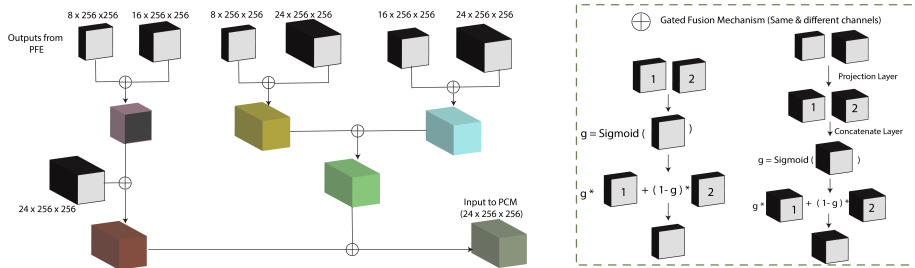


Figure 2: Illustration of the Patch Fusion Module (PFM), where multi-scale feature maps are combined using a gated fusion mechanism.

4 Experimental Setup

4.1 Datasets

For evaluation, we use the publicly available NIH-AAPM 2016 Mayo Low-Dose Computed Tomography (LDCT) dataset [17]. This dataset consists of paired low-dose CT (LDCT) and normal-dose CT (NDCT) abdominal scans acquired using a Siemens SOMATOM Flash scanner in the portal venous phase. For the main evaluation, we use images reconstructed with a 3 mm slice thickness and the B30 reconstruction kernel. The dataset contains CT scans from 10 patients, each with a varying number of slices.

Due to the limited number of patients, we adopt a patient-wise 5-fold cross-validation strategy to ensure that the evaluation is not biased toward any particular subset of the data. Beyond the primary evaluation, we also assess the robustness and generalizability of the proposed method by conducting experiments on different slice thicknesses, reconstruction kernels, and cross-dataset validation on a General Electric (GE) scanner without any fine-tuning. For these experiments we only trained and evaluated on fold-5 dataset to expedite experimentation cycle.

For cross-dataset validation, synthetic noise (Poisson noise) is added, and the model is trained on Siemens-based scanner data and directly tested on GE-based scanner images to evaluate its ability to generalize across scanner types and noise characteristics.

4.2 Preprocessing

CT images contain raw pixel intensity values that depend on scanner-specific acquisition parameters. To obtain a standardized and scanner-independent representation, the raw pixel values are converted to Hounsfield Units (HU) using the formula (2).

$$HUImg = Img * RescaleSlope + RescaleIntercept \quad (1)$$

For abdominal LDCT imaging, clinically meaningful HU values typically lie

within the range of -160 to 240 . Therefore, the images are clipped to this range and subsequently normalized to $[0, 1]$. This preprocessing strategy is applied consistently for both training and testing across all evaluated methods to ensure a fair comparison. To further evaluate robustness, we also test the trained models on different HU window settings, as described in a subsequent section.

4.3 Training

All models are implemented using PyTorch. We employ the L1 loss function (2) and optimize the network parameters using the Adam optimizer with a cosine annealing learning rate schedule. The initial learning rate is set to $1e^{-2}$, with a minimum learning rate $\eta_{min} = \frac{1e^{-2}}{160}$. Training is performed with a batch size of 1 for 80 epochs on an NVIDIA RTX 5000 Ada Generation GPU. The total training time for the proposed model is approximately 56 minutes.

$$Loss = \sum_{i=1}^N |y_{gt} - y_{pred}| \quad (2)$$

4.4 Evaluation Metrics

Denoising performance is evaluated using peak signal-to-noise ratio (PSNR), structural similarity index measure (SSIM), and root mean square error (RMSE). Results are reported as mean \pm standard deviation across the five cross-validation folds.

5 Results

Table 1 presents the comparative quantitative evaluation of different algorithms on the 2016 Mayo LDCT dataset using five-fold cross-validation. PatchDenoiser consistently outperforms all competing methods, including advanced approaches such as CNCL and CTFormer, in terms of PSNR and SSIM. It should be noted that CTFormer was trained for only 200 epochs due to its substantially longer training time. Although the original authors mention both 200 and 4000 epochs in their codebase, training CTFormer for additional epochs may or may not lead to improved performance. Importantly, the superior performance of PatchDenoiser is consistently observed across all folds, indicating robustness and reduced sensitivity to inter-patient variations. A qualitative comparison of the denoised results with zoomed-in regions of interest is shown in Figure 3, illustrating the visual advantages of PatchDenoiser.

Table 2 provides a comparison of model parameters, model size, and FLOPs among the evaluated deep learning based algorithms. Parameters and FLOPs are computed under inference settings to reflect realistic deployment conditions. Notably, PatchDenoiser exhibits one of the lowest training and inference times among all methods. This is particularly important, as image denoising typically

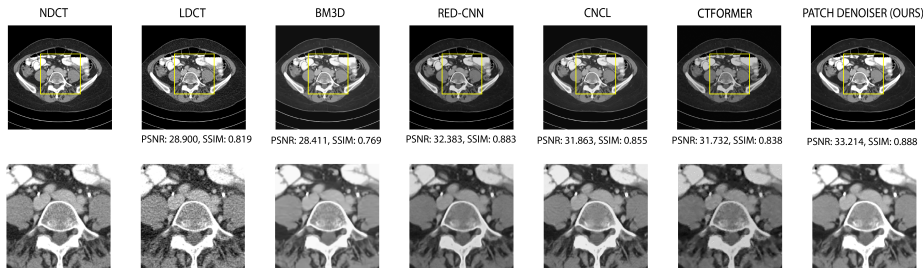


Figure 3: Qualitative comparison of denoised abdomen LDCT images on the 2016 Mayo dataset. Zoomed-in regions of interest highlight differences in noise suppression and structural detail preservation among the evaluated methods.

Table 1: Quantitative comparison of denoising performance (mean \pm std) on the 2016 Mayo LDCT dataset using five-fold cross-validation.

| Algorithms | | LDCT | BM3D | RED-CNN | CNCL | CTFormer | PatchDenoiser(Ours) |
|------------|------|--------------------|--------------------|--------------------|--------------------|--------------------|--------------------------------------|
| Fold-1 | PSNR | 28.177 \pm 1.950 | 29.960 \pm 2.246 | 32.197 \pm 1.340 | 32.495 \pm 1.520 | 31.597 \pm 1.525 | 32.949 \pm 1.532 |
| | SSIM | 0.860 \pm 0.041 | 0.882 \pm 0.040 | 0.903 \pm 0.029 | 0.901 \pm 0.031 | 0.891 \pm 0.029 | 0.908 \pm 0.029 |
| Fold-2 | PSNR | 26.702 \pm 2.065 | 28.541 \pm 2.477 | 30.976 \pm 1.711 | 31.400 \pm 1.822 | 29.743 \pm 1.569 | 31.567 \pm 1.813 |
| | SSIM | 0.787 \pm 0.065 | 0.821 \pm 0.060 | 0.856 \pm 0.044 | 0.858 \pm 0.045 | 0.834 \pm 0.044 | 0.861 \pm 0.045 |
| Fold-3 | PSNR | 28.690 \pm 1.807 | 30.586 \pm 2.194 | 32.449 \pm 1.205 | 32.675 \pm 1.329 | 31.857 \pm 1.193 | 33.291 \pm 1.339 |
| | SSIM | 0.831 \pm 0.047 | 0.863 \pm 0.044 | 0.889 \pm 0.029 | 0.884 \pm 0.030 | 0.862 \pm 0.034 | 0.896 \pm 0.028 |
| Fold-4 | PSNR | 25.890 \pm 2.343 | 27.504 \pm 2.755 | 30.400 \pm 1.692 | 30.329 \pm 1.930 | 29.564 \pm 1.790 | 30.976 \pm 1.940 |
| | SSIM | 0.796 \pm 0.063 | 0.823 \pm 0.059 | 0.856 \pm 0.047 | 0.850 \pm 0.051 | 0.842 \pm 0.045 | 0.861 \pm 0.048 |
| Fold-5 | PSNR | 26.767 \pm 1.422 | 28.441 \pm 1.769 | 31.123 \pm 1.265 | 31.371 \pm 1.306 | 30.284 \pm 1.282 | 31.525 \pm 1.423 |
| | SSIM | 0.801 \pm 0.043 | 0.831 \pm 0.039 | 0.864 \pm 0.029 | 0.866 \pm 0.030 | 0.845 \pm 0.034 | 0.868 \pm 0.030 |

serves as a preprocessing or intermediate step within a larger AI pipeline. Another major advantage of PatchDenoiser lies in its efficiency in terms of both parameter count and computational complexity. Specifically, PatchDenoiser uses approximately $9.25\times$ and $235\times$ fewer parameters than CNN and GAN-based methods, respectively. In addition, a substantial reduction in Floating-point Operations Per Second (FLOPs) is observed, with PatchDenoiser requiring approximately $27\times$ fewer GFLOPs. This efficiency advantage is further reflected in the energy-per-inference metric, which is calculated as GFLOPs divided by 20 W, assuming an average energy requirement of 20 W per 1 GFLOP. These results clearly demonstrate that PatchDenoiser not only achieves superior denoising performance but also offers high computational and energy efficiency.

Table 2: Comparison of model complexity and computational efficiency for the evaluated denoising methods. Parameters and FLOPs are measured under inference settings, and energy per inference is estimated from GFLOPs.

| Algorithms | Train time (mins) | Infer time (s) | Params(M) | Size(MB) | FLOPs(GFlops) | Energy per inference(GFlops/Watt) |
|---------------|-------------------|----------------|-----------|----------|---------------|-----------------------------------|
| RED-CNN | 50 | 0.025 | 1.85 | 7.05 | 458 | 23 |
| CNCL | 800 | 0.018 | 47 | 177 | 290 | 15 |
| CTFormer | 90 | 0.11 | 1.45 | 6.3 | 85 | 4.5 |
| PatchDenoiser | 56 | 0.006 | 0.2 | 0.75 | 17 | 0.85 |

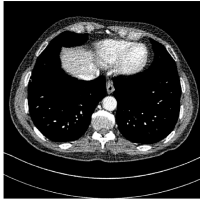
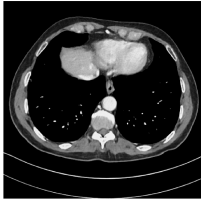
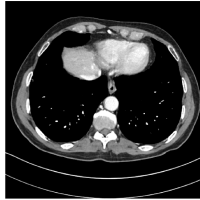
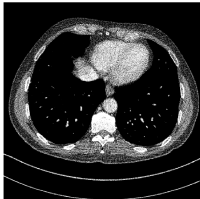
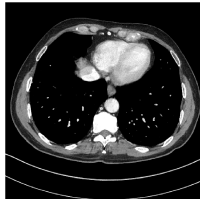
| | LDCT | RED-CNN | PATCH DENOISER (OURS) |
|---------|---|---|---|
| 1mm B30 |  PSNR: 25.280, SSIM: 0.865 |  PSNR: 29.929, SSIM: 0.900 |  PSNR: 30.130, SSIM: 0.905 |
| 1mm D45 |  PSNR: 17.788, SSIM: 0.788 |  PSNR: 23.293, SSIM: 0.827 |  PSNR: 23.344, SSIM: 0.833 |
| 3mm D45 |  PSNR: 19.661, SSIM: 0.751 |  PSNR: 25.458, SSIM: 0.796 |  PSNR: 25.568, SSIM: 0.804 |

Figure 4: Qualitative denoising results under different slice thicknesses and reconstruction kernels on the 2016 Mayo LDCT dataset.

5.1 Evaluation on Variations in Hounsfield Unit (HU) Window, Slice Thickness, and Reconstruction Kernel

To ensure that PatchDenoiser is robust and performs consistently under different imaging conditions, we trained and evaluated the model using a wider HU window ranging from -1000 to $+1000$, as well as different slice thicknesses and reconstruction kernels available in the 2016 Mayo LDCT dataset, namely 1 mm B30, 3 mm B30, 1 mm D45, and 3 mm D45. Tables 3 and 4 present the corresponding results and clearly indicate that PatchDenoiser achieves superior performance compared to other CNN-based models. In these experiments, we restrict comparisons to RED-CNN in the interest of training time and computational feasibility. Figure 4 shows qualitative denoising results under different slice thicknesses and reconstruction kernels, demonstrating the robustness of PatchDenoiser across varying acquisition settings.

Table 3: Quantitative denoising performance using an extended Hounsfield Unit (HU) window (-1000 to +1000) on the 2016 Mayo LDCT dataset.

| Algorithms | PSNR | SSIM |
|---------------|--------------------------------------|-------------------------------------|
| RED-CNN | 43.277 ± 1.390 | 0.968 ± 0.008 |
| PatchDenoiser | 43.464 ± 1.522 | 0.969 ± 0.009 |

Table 4: Quantitative denoising performance under varying slice thicknesses and reconstruction kernels on the 2016 Mayo LDCT dataset. Results are reported for 1 mm and 3 mm slice thickness with B30 and D45 kernels.

| Algorithms | | RED-CNN | PatchDenoiser |
|------------|------|--------------------|--------------------------------------|
| 1mm B30 | PSNR | 27.176 ± 1.270 | 27.332 ± 1.303 |
| | SSIM | 0.789 ± 0.042 | 0.794 ± 0.043 |
| 3mm B30 | PSNR | 31.123 ± 1.265 | 31.525 ± 1.423 |
| | SSIM | 0.864 ± 0.029 | 0.868 ± 0.030 |
| 1mm D45 | PSNR | 20.815 ± 1.196 | 20.862 ± 1.202 |
| | SSIM | 0.677 ± 0.058 | 0.685 ± 0.062 |
| 3mm D45 | PSNR | 24.948 ± 1.232 | 25.065 ± 1.239 |
| | SSIM | 0.748 ± 0.049 | 0.753 ± 0.051 |

5.2 Cross-Dataset Generalization

To further evaluate the generalization capability of PatchDenoiser, we tested the model without fine-tuning on abdomen LDCT scans acquired using a General Electric (GE) scanner from the LDCT Cancer Archive dataset [18]. For consistency, comparisons are again limited to RED-CNN. The results, summarized in Table 5, demonstrate that PatchDenoiser achieves better generalization performance under cross-scanner and cross-dataset conditions.

6 Ablation Studies

We also performed ablation studies to identify an optimal architecture for the proposed framework. Table 6 summarizes the ablation experiments conducted. In particular, we investigate the impact of different patch sizes and the use of

Table 5: Cross-dataset generalization performance on abdomen LDCT scans from the LDCT Cancer Archive dataset acquired using a General Electric (GE) scanner.

| Algorithms | | RED-CNN | PatchDenoiser |
|--------------|------|--------------------------------------|--------------------------------------|
| Val(Siemens) | PSNR | 38.504 ± 0.682 | 38.489 ± 1.140 |
| | SSIM | 0.973 ± 0.007 | 0.973 ± 0.007 |
| Test(GE) | PSNR | 37.550 ± 0.908 | 37.744 ± 0.839 |
| | SSIM | 0.970 ± 0.007 | 0.972 ± 0.006 |

Table 6: Ablation Studies

| Configuration | Patch Size | Fusion | PSNR | SSIM |
|-----------------|------------|--------|--------|-------|
| Baseline | 32/128/512 | Gated | 31.480 | 0.868 |
| Small patches | 16/64/256 | Gated | 31.434 | 0.868 |
| No Gated Fusion | 32/128/512 | Concat | 31.416 | 0.859 |

gated fusion. Selecting appropriate patch sizes is crucial for PatchDenoiser, as the goal is to reduce the number of parameters while maintaining strong denoising performance. Notably, in some cases, we observe that increasing the model size does not necessarily lead to improved performance, highlighting the importance of efficient architectural design.

7 Discussion

The results demonstrate that PatchDenoiser achieves competitive denoising performance while maintaining high computational efficiency. This represents an important contribution to architectural design, as many recent denoising models rely on large-scale networks with substantial computational and energy demands, which are increasingly unfavorable from both economic and environmental perspectives. PatchDenoiser offers a good trade-off by explicitly decomposing the denoising process into local texture modeling and global context aggregation, combined with an efficient multi-scale patching strategy and spatially aware feature fusion.

In contrast to conventional encoder-based or patch-based architectures, which often reduce spatial resolution and consequently discard important structural information, PatchDenoiser preserves spatial dimensions throughout the feature extraction process. This design minimizes information loss during feature fusion and enables effective local-to-global interactions while maintaining spatial consistency in the reconstructed images.

Beyond its strong quantitative performance, PatchDenoiser demonstrates notable robustness and reduced sensitivity to the training regime. Variations in slice thickness and reconstruction kernels do not diminish its competitive advantage, highlighting its stability across common acquisition settings. Moreover, generalization is a critical requirement for medical imaging applications. In this respect, PatchDenoiser was evaluated on a dataset acquired using a GE scanner without any fine-tuning and was found to maintain stable performance, indicating strong cross-scanner generalizability.

One contributing factor to this robustness may be the relatively small number of learnable parameters, which reduces the risk of overfitting and promotes improved generalization to previously unseen imaging domains.

Despite these advantages, PatchDenoiser also has certain limitations. The choice of patch size and the number of patch scales play a critical role in overall performance. Although patch sizes are not explicitly hard-coded and are instead determined adaptively based on image dimensions (e.g., by dividing

the image size by fixed ratios), performance degradation is observed when very small patches are used. In addition, the selection of an appropriate depth for the Patch Feature Extractor (PFE) remains partially empirical, and further systematic investigation is required to fully optimize this design choice.

Patch boundary artifacts may also arise during the feature fusion process. In this study, the proposed Patch Consolidator Module (PCM) was effective in mitigating such artifacts. However, patch fusion remains a challenging aspect of patch-based denoising architectures and warrants further research.

Moreover, PatchDenoiser is most effective in scenarios where local contextual information dominates and long-range global dependencies are less critical. As a result, its applicability may be limited for tasks that require extensive global modeling. However, since medical image denoising is predominantly governed by local anatomical structures and textures, this architectural choice is well aligned with the intrinsic characteristics of the problem domain.

In the context of medical image denoising, PatchDenoiser offers a clear practical advantage. While large transformer- or GAN-based models may achieve marginally higher PSNR or SSIM values, their substantially increased architectural complexity and parameter counts often lead to diminishing performance returns. PatchDenoiser is also less sensitive to dataset size and variations, a limitation commonly observed in large-scale models, which can limit their robustness in clinical settings.

Given that denoising typically functions as a preprocessing step within a broader clinical AI pipeline, lightweight and energy-efficient models are often preferable to ensure scalability and ease of deployment. From this perspective, PatchDenoiser offers a good trade-off between denoising performance, computational efficiency, and robustness, making it well suited for practical clinical applications.

8 Conclusion

In this work, we presented PatchDenoiser, a parameter- and energy-efficient multi-scale patch-based framework for medical image denoising. By explicitly separating local texture extraction from global context aggregation and employing spatially aware feature fusion, the proposed model achieves competitive denoising performance while maintaining an ultra-lightweight architecture. Extensive experiments on the 2016 Mayo Low-Dose CT dataset demonstrate robustness to variations in Hounsfield unit windows, slice thickness, and reconstruction kernels, as well as strong generalization across scanners.

To the best of our knowledge, PatchDenoiser represents one of the most computationally efficient medical image denoising frameworks to date, offering a favorable balance among denoising performance, computational cost, and robustness. These characteristics make it particularly well suited for integration into practical clinical AI pipelines.

Future work will focus on further enhancing the adaptability and generalization of the proposed framework, including the development of dynamic

patch selection strategies and the incorporation of mechanisms to better capture long-range global dependencies. Extending PatchDenoiser to additional imaging modalities and integrating it into end-to-end clinical AI pipelines also represent promising directions. Furthermore, exploring model compression and quantization techniques may further improve energy efficiency and facilitate deployment in real-world clinical environments.

References

- [1] V. A. Ferdinand, V. Nawir, G. E. Henry, Anderies, and A. A. Santoso Gunawan, ‘Effect of Image Enhancement in CNN-Based Medical Image Classification: A Systematic Literature Review’, in 2022 5th International Conference on Information and Communications Technology (ICOIACT), Aug. 2022, pp. 87–92. doi: 10.1109/ICOIACT55506.2022.9972030.
- [2] N. Vannadil and P. Kokil, ‘Noise and performance analysis on fundus images with CNN and transformer models’, in 2023 IEEE 7th Conference on Information and Communication Technology (CICT), Dec. 2023, pp. 1–6. doi: 10.1109/CICT59886.2023.10455148.
- [3] S. Kaur, J. Singla, Nikita, and A. Singh, ‘Review on Medical Image Denoising Techniques’, in 2021 International Conference on Innovative Practices in Technology and Management (ICIPTM), Feb. 2021, pp. 61–66. doi: 10.1109/ICIPTM52218.2021.9388367.
- [4] N. Nazir, A. Sarwar, and B. S. Saini, ‘Recent developments in denoising medical images using deep learning: An overview of models, techniques, and challenges’, *Micron*, vol. 180, p. 103615, May 2024, doi: 10.1016/j.micron.2024.103615.
- [5] A. Buades, B. Coll, and J.-M. Morel, ‘Non-Local Means Denoising’, *Image Processing On Line*, vol. 1, pp. 208–212, 2011.
- [6] K. Dabov, A. Foi, V. Katkovnik, and K. Egiazarian, ‘Image denoising by sparse 3D transform-domain collaborative filtering’.
- [7] H. Chen et al., ‘Low-Dose CT with a Residual Encoder-Decoder Convolutional Neural Network (RED-CNN)’, *IEEE Trans. Med. Imaging*, vol. 36, no. 12, pp. 2524–2535, Dec. 2017, doi: 10.1109/TMI.2017.2715284.
- [8] S. M. A. Sharif, R. A. Naqvi, and M. Biswas, ‘Learning Medical Image Denoising with Deep Dynamic Residual Attention Network’, *Mathematics*, vol. 8, no. 12, Art. no. 12, Dec. 2020, doi: 10.3390/math8122192.
- [9] S. M. A. Sharif, R. A. Naqvi, and W.-K. Loh, ‘Two-Stage Deep Denoising With Self-Guided Noise Attention for Multimodal Medical Images’, *IEEE Transactions on Radiation and Plasma Medical Sciences*, vol. 8, no. 5, pp. 521–531, May 2024, doi: 10.1109/TRPMS.2024.3380090.

- [10] G. Dong, Y. Ma, and A. Basu, ‘Feature-Guided CNN for Denoising Images From Portable Ultrasound Devices’, *IEEE Access*, vol. 9, pp. 28272–28281, 2021, doi: 10.1109/ACCESS.2021.3059003.
- [11] S. Yang, Q. Pu, C. Lei, Q. Zhang, S. Jeon, and X. Yang, ‘Low-dose CT denoising with a high-level feature refinement and dynamic convolution network’, *Medical Physics*, vol. 50, no. 6, pp. 3597–3611, 2023, doi: 10.1002/mp.16175.
- [12] M. Geng et al., ‘Content-Noise Complementary Learning for Medical Image Denoising’, *IEEE Transactions on Medical Imaging*, vol. 41, no. 2, pp. 407–419, Feb. 2022, doi: 10.1109/TMI.2021.3113365.
- [13] Z. Huang, J. Zhang, Y. Zhang, and H. Shan, ‘DU-GAN: Generative Adversarial Networks With Dual-Domain U-Net-Based Discriminators for Low-Dose CT Denoising’, *IEEE Transactions on Instrumentation and Measurement*, vol. 71, pp. 1–12, 2022, doi: 10.1109/TIM.2021.3128703.
- [14] D. Mishra, S. Chaudhury, M. Sarkar, and A. S. Soin, ‘Ultrasound Image Enhancement Using Structure Oriented Adversarial Network’, *IEEE Signal Processing Letters*, vol. 25, no. 9, pp. 1349–1353, Sep. 2018, doi: 10.1109/LSP.2018.2858147.
- [15] H. Yin and S. Ma, ‘CSformer: Cross-Scale Features Fusion Based Transformer for Image Denoising’, *IEEE Signal Processing Letters*, vol. 29, pp. 1809–1813, 2022, doi: 10.1109/LSP.2022.3199145.
- [16] D. Wang, F. Fan, Z. Wu, R. Liu, F. Wang, and H. Yu, ‘CTformer: Convolution-free Token2Token Dilated Vision Transformer for Low-dose CT Denoising’, *Phys. Med. Biol.*, vol. 68, no. 6, p. 065012, Mar. 2023, doi: 10.1088/1361-6560/acc000.
- [17] C. H. McCollough et al., ‘Low-dose CT for the detection and classification of metastatic liver lesions: Results of the 2016 Low Dose CT Grand Challenge’, *Med Phys*, vol. 44, no. 10, pp. e339–e352, Oct. 2017, doi: 10.1002/mp.12345.
- [18] T. R. Moen et al., ‘Low-dose CT image and projection dataset’, *Med Phys*, vol. 48, no. 2, pp. 902–911, Feb. 2021, doi: 10.1002/mp.14594.